Applied Physics B (2026) 132:12
https://doi.org/10.1007/s00340-025-08616-7

Applied Physics B
Lasers and Optics

RESEARCH

Terahertz generation from chirped and delayed laser pulses in a periodically poled lithium niobate waveguide

Ilyes Betka[1] · Moise Deroh[2,3] · Simon Dubuis[4,5] · Gabriel Taton[1] · Frédéric Fauquet[1] · Moses Eshovo Ojo[1] · Coralie Fourcade-Dutin[1] · Hervé Maillotte[2] · Vincent Rodriguez[4] · Mathieu Chauvet[2] · Patrick Mounaix[1] · Damien Bigourd[1]

Received: 24 September 2025 / Accepted: 15 December 2025

Abstract
THz generation from chirped and delayed laser pulses using periodically poled lithium niobate (PPLN) traditionally requires high-energy sources and bulky PPLN crystals. However, for compact, integrated, and miniaturized THz-based applications, such systems must be downsized. In this work, we numerically and experimentally demonstrate THz generation in a PPLN waveguide with a cross-section of 500×500 μm^2, pumped with low pulse energies in the microjoule range at a wavelength of 1 μm. Simulations show that tightly focused optical pulses in this configuration achieve significantly higher THz generation efficiency compared to collimated pumping. For a propagation length of 1.6 cm, optimal parameters are identified as a pulse duration of 5 ps and a pump energy between 0.5 and 1 μJ. Experimental validation confirms these findings, yielding a narrowband THz spectrum centered around 488 GHz. This work opens new perspectives for the development of efficient, integrated THz sources for advanced applications in THz photonics, spectroscopy, and high-speed communications.

1 Introduction

Terahertz (THz) frequencies are electromagnetic waves spanning from 0.1 to 10 THz. These waves have a wide range of applications, including imaging [1, 2], spectroscopy [3, 4], THz-based particle accelerators [5], and communication [6]. Several THz generation techniques have been explored such as optical rectification [7], photoconductive antennas [8], polariton scattering [9], and difference frequency mixing using chirped and delayed laser pulses [10]. Among these, chirped and delayed laser pulse (CADLP) methods stand out for producing narrowband THz in the 0–1 THz range with high efficiency [11, 12], tunability and the capability of generating strong peak electric fields [10]. Lithium Niobate (LN) is an attracting material for THz generation [13] due to high second-order nonlinear response [14], infrared transparency [15] and robust mechanical properties [16]. However, a major limitation of using LN with CADLD techniques is the phase mismatch between the THz and optical waves [11], which significantly reduces the conversion efficiency. Periodically Poled Lithium Niobate (PPLN) addresses this challenge by enabling quasi-phase matching [17] for narrowband THz generation, significantly enhancing THz generation efficiency [11, 12, 18].

To date, THz generation from PPLN using CADLP has relied on bulky setups and high-energy pump sources. Previous studies [11, 12] demonstrated THz generation using large scale PPLN crystal pumped by Ti:sapphire lasers at very high pulse energies of 1–5 J. While effective for high field THz generation, these systems are not suited for developing high repetition rate, miniaturized, compact, and portable THz applications. To overcome these limitations, reducing both pump energy and PPLN dimensions using waveguide geometries becomes essential. Waveguides not

✉ Ilyes Betka
Ilyes.betka@u-bordeaux.fr

[1] Laboratoire IMS, UMR CNRS 5218, Université de Bordeaux, 33400 Talence, France

[2] Université Marie et Louis Pasteur, CNRS, Institut FEMTO-ST, 25000 Besançon, France

[3] Laboratoire d'Instrumentation, Image et Spectroscopie (L2IS), Institut National Polytechnique Félix Houphouët Boigny (INP-HB), BP 1093, Yamoussoukro, Côte d'Ivoire

[4] Institut des Sciences Moléculaires, UMR CNRS 5255, Université de Bordeaux, 33405 Talence Cedex, France

[5] NLOPTICS, Cité Numérique, 33130 Bègles, France

Published online: 05 January 2026

only allow for a compact footprint but also confine the THz field along the propagation direction, reducing diffraction and enhancing field strength [19]. This approach paves the way for miniaturized THz sources operating at high repetition rates and integrated on chip.

In this study, we report for the first time THz generation from PPLN using CADLP technique, which combines low pump energy in the µJ or sub-µJ range with high repetition rate-higher than those provided by a Ti:Sapphire laser- and waveguide geometry. This configuration is designed to only guide the THz waves. Our investigation began with numerical simulations based on coupled wave equations accounting for nonlinear interactions between terahertz and optical waves, including pump depletion, cascaded difference frequency generation, self-phase modulation (SPM), cascaded second harmonic generation, and Raman processes, as well as the overlap integral between the pump and THz fields. We analyzed the efficiency of a 16 mm long PPLN waveguide with a 223 µm poling period, varying pulse duration, beam geometry (focused vs collimated) and pump energy.

Guided by these simulations, we developed a dedicated PPLN and characterized their properties. Then we experimentally implemented the optimal parameters and demonstrated THz generation centered at 488 GHz with a narrow bandwidth of 180 GHz, in excellent agreement with numerical predictions. This bandwidth is qualified as narrow in comparison with an ultra-short pulse excitation that provides a THz pulse with few THz bandwidth [9]. The employed pump conditions are comparable to those achievable with compact, portable fiber-based lasers and emerging on-chip integrated laser sources, paving the way toward fully integrated and miniaturized THz systems based on PPLN waveguides. Our approach thus provides a powerful platform for realizing compact THz sources applicable to wireless communication [20], on-chip spectroscopy [21], and signal-processing platforms [22].

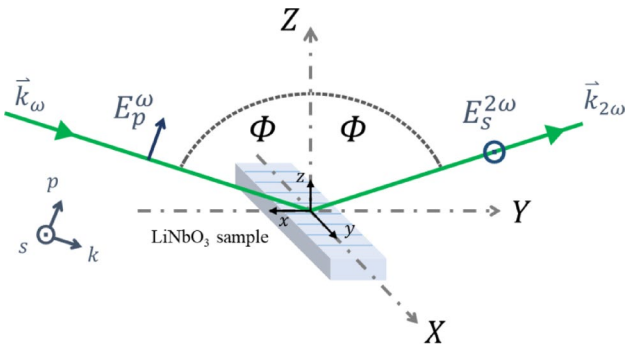

Fig. 1 Schematic representation of the orientation of the PPLN with respect to the laboratory reference frame (XYZ) and the crystallographic frame (xyz). The incident beam is shown with an p-polarized incident beam, and is analyzed using a s-polarized configuration

2 Materials and methods

2.1 PPLN fabrication

The waveguide, designed for THz radiation, consists of a square $LiNbO_3$ core surrounded by an air cladding. It is based on a type-0 difference frequency mixing configuration with both pump and generated beam polarized along the extraordinary axis to exploit the strongest d_{33} nonlinear coefficient of $LiNbO_3$. The fabrication process [23, 24] starts with the electric poling of a 500 µm thick undoped congruent z-cut $LiNbO_3$ wafer with the chosen poling period of 223 µm. Waveguides are then diced with a precision saw equipped with a polishing diamond blade. The dicing process provides facets with a roughness of about 0.5 nm.

2.2 PPLN characterization

PPLN samples were analyzed using a custom second-harmonic generation reflectometer (R-SHG) [25] based on a reflection geometry with controlled incident polarization and spatial positioning. A femtosecond laser centered at 1030 nm, with a pulse duration of 250 fs and a repetition rate of 54 MHz is used as the excitation source. The beam firstly passed through a variable neutral density filter to adjust the incident power and is then directed through a set of a rotating half-wave plate and a fixed quarter-wave plate to define the incident polarization state. The beam is subsequently focused onto the sample surface, resulting in a spot size on the order of a few microns. The oblique incident angle is fixed to a grazing angle of 70° (vertical plane of incidence) according to the vertical Z axis (Fig. 1), ensuring thus an excellent sensitivity to both in-plane and out-of-plane nonlinear responses of the interface. More details can be found in [25]. The technique thus provides non-destructive, non-contact, and label-free contrast, ideal for mapping crystalline quality, domain orientation, and structural inhomogeneities across a surface. When combined with spatial scanning, R-SHG becomes a powerful tool for 2D cartography of the nonlinear response, enabling the visualization of local variations in the effective nonlinear susceptibility with micrometer-scale resolution. The sample is mounted on a computer-controlled 3-axis translation stage (X, Y, Z lab frame), allowing for precise positioning and depth scanning (Z-scan) to optimize the focus at the air/sample interface. The reflected second harmonic (2ω) signal is filtered from the fundamental (ω) signal using both a short-pass filter and a band-pass optical filter centered at 520 nm (FWHM ≈ 40 nm), ensuring spectral purity. The SHG signal is detected by a photomultiplier tube. A polarization analyzer placed in the collection path allows for polarization resolved detection, enabling the analysis of different tensor components

of $\chi^{(2)}$ via specific polarization combinations (e.g., s-in/s-out, p-in/p-out).In the laboratory reference frame, a linear horizontal polarization, denoted {s}, is entirely aligned with the X-axis, while a linear vertical polarization, denoted {p}, exhibits components along both the Y and Z directions.

The collected second-harmonic intensity $\boldsymbol{I}_{2\omega}$ is proportional to the square of the incident intensity $\boldsymbol{I}_{\omega}$, and to the square of the second-order nonlinear susceptibility $\boldsymbol{\chi}^{(2)}$, as expressed by:

$$I_{2\omega} \propto \left|\chi^{(2)}\right|^2 \cdot I_{\omega}^2$$

In the case of $LiNbO_3$, the point-group symmetry to consider in the Schoenflies notation is C_{3v} (3 m in International notation), which defines the non-zero components of the second-order nonlinear susceptibility tensor $\chi^{(2)}$. The nonlinear polarization $\mathbf{P^{(2)}}$ components at the frequency 2ω can be expressed as a function of the electric field components of the signal at the frequency ω:

$$\begin{aligned} P_x &= 2d_{15}E_xE_z - 2d_{22}E_yE_x \\ P_y &= 2d_{15}E_yE_z + d_{22}\left(E_y^2 - E_x^2\right) \\ P_z &= d_{31}\left(E_x^2 + E_y^2\right) + d_{33}E_z^2 \end{aligned} \quad (1)$$

where $d_{22} = \chi^{(2)}_{yyy}$, $d_{31} = \chi^{(2)}_{zxx} \approx d_{15} = \chi^{(2)}_{xxz}$, and $d_{33} = \chi^{(2)}_{zzz}$. The SHG coefficients d_{22} and $d_{31} \approx d_{15}$ are typically in the order of a few pm/V, while d_{33} is significantly larger [26]. Note these SHG coefficients were measured at 1.058 µm and comes essentially from the electronic NLO response, whereas DFG processes involve mostly the phonon (nucleus) contributions. However, all these second-order processes have the same symmetry and spatial addition, d_{33} is particularly sensitive to composition variations (ratio Li/Nb) [26] and crystalline defects, making it an excellent indicator of structural quality.

For a z-cut $LiNbO_3$ crystal, the sample surface corresponds to the (x, y) plane. A simple overlap between the two coordinate systems, (x, y, z) and (− Y, X, Z) of the laboratory frame, is achieved when the crystallographic axes of the crystal are aligned in this way. As illustrated in Fig. 1, the periodic axis lies along the crystallographic y-axis, and overlaps the X-axis. For spatial mapping (R-SHG cartography), the sample is moved along X (y) and Y (x) directions, over predefined regions with step sizes of 2 µm in the X direction, and 10 µm in the Y direction. At each position (pixel), the SHG intensity is recorded, allowing for the generation of two-dimensional maps reflecting local variations in nonlinear optical response.

Under these frame orientations, and from Eq. 1, the s-polarized NLO response does not probe the main component d_{33} but the minor components, d_{22} and $d_{15} \approx d_{31}$, which is a good point for the contrast. Then, the ferroelectrics domains will provide intensity, through $d_{22} = \chi^{(2)}_{yyy}$ and $d_{15} = \chi^{(2)}_{xxz}$. In addition, the electric-field-induced second harmonic (EFISH) response located at the wall of the domains, will provide thus an additional localized EFISH intensity with an effective $d_{15} = \chi^{(2)}_{xxz}$ type character. Actually, considering the cartesian susceptibilities for clarity purpose, a s-polarization will give the following contributions from the domains and walls

$$P_y = \left[2\chi^{(2)}_{yyz}E_yE_z + \chi^{(2)}_{yyy}\left(E_y^2 - E_x^2\right)\right]_{Domains} + \left[2\chi^{(3)}_{yyzz}E_yE_zE_z^{DC}\right]_{Walls} \quad (2)$$

where the EFISH term $\chi^{(3)}_{yyzz}E_yE_zE_z^{DC}$ corresponds to an effective $\chi^{(2)}_{yzz} = d_{15}$ term. Considering a perfect alignment, a p-polarized incident beam ($E_x \neq 0$, $E_z \neq 0$, $E_y = 0$) will only probe the domains contribution with the $\chi^{(2)}_{yyy}E_x^2$ term. However, a slight rotation along the vertical z-axis will give a weak enough $E_y \neq 0$ contribution to the p-s SHG signal, so that the domain will give an almost constant intensity while the wall domains will exhibit an additional intensity as reported in Fig. 2. Under these conditions, a periodic pattern is evidenced with a measured pitch of 231 ± 8 µm. As this measured period lies within the acceptable tolerance range of the designed poling period, the inversion period of 223 µm used as input for the fabrication was retained in the simulations in the next sections.

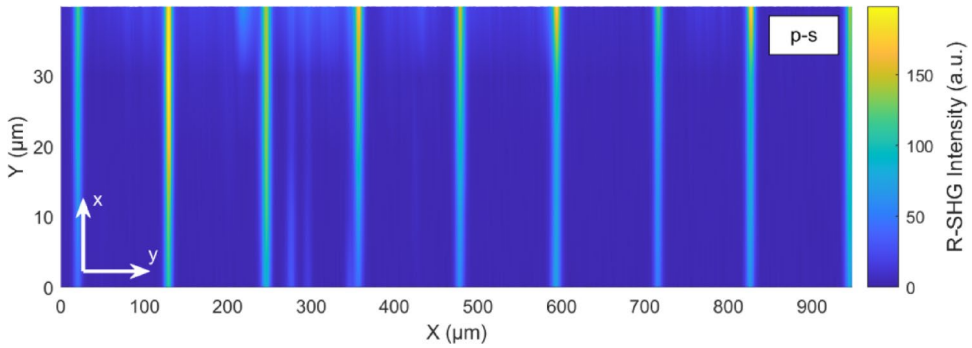

Fig. 2 R-SHG mapping of the PPLN sample under p-s configuration, with respect to the crystallographic y-axis. The poled periodicity is nicely evidenced

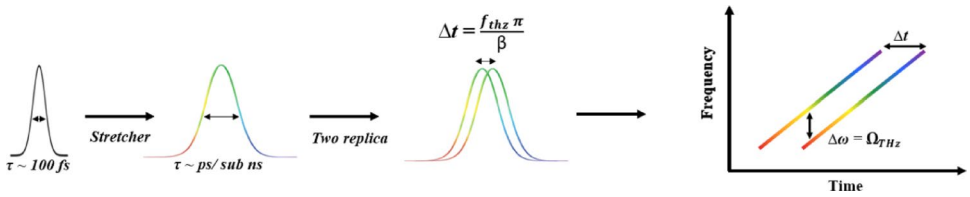

Fig. 3 Chirp and delay concept. τ: pulse duration; Δt: optical delay; f_{THz}: THz frequency; β: linear chirp; Δω: instantaneous angular frequency difference; Ω: THz angular frequency

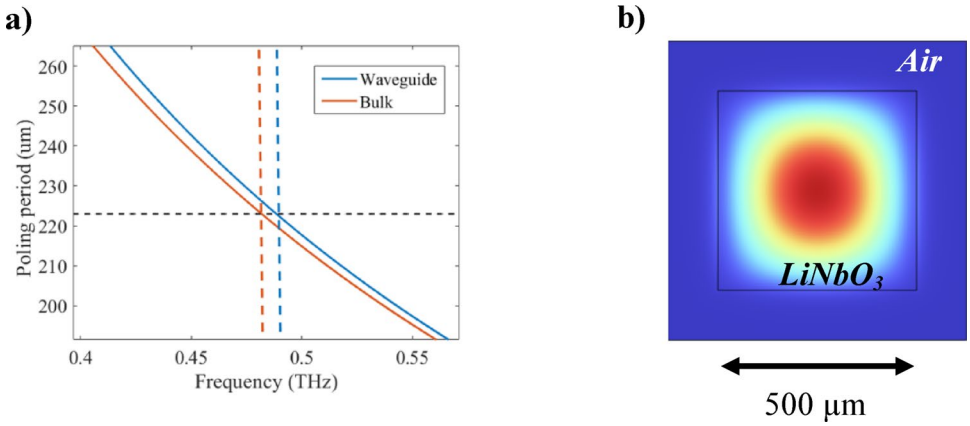

Fig. 4 **a** Poling period as a function of the THz frequency using Eq. (4). **b** Spatial mode profile of $LiNbO_3$ at 480 GHz

Signal features are also observed within the half-periods, corresponding to domain wall regions. These contrasts suggest that domain inversion occurs both at the edges of the periods and at their center, indicating the presence of internal domain boundaries.

2.3 Chirped and delayed laser pulses technique

The CADLP technique has been extensively used for generating mid-infrared pulses in nonlinear crystals [27], and for producing narrowband THz pulses using photoconductive antennas [8, 28]. In the latter application, the method was later extended to nonlinear crystals like LN by employing tilted optical pulse wavefronts [10], and subsequently to PPLN as well [11, 12]. As illustrated in Fig. 3, the CADLP approach involves temporally stretching a femtosecond pulse with a sufficiently broad spectral bandwidth, increasing its duration from few hundred of femtoseconds to the picosecond or even nanosecond range. This generates a chirped pulse characterized by a chirp rate β, with an instantaneous frequency that increases monotonically over time. The chirped pulse is then split into two replicas, which are recombined interferometrically with a relative time delay Δt. Assuming a linear chirp, the instantaneous frequencies of the two pulses are given by $\omega(t)=\omega_0+2\beta t$ and $\omega(t)=\omega_0+2\beta t+2\beta\Delta t$, respectively, where ω_0 is the central angular frequency. The difference in instantaneous angular frequency, Δω, is determined by the delay and the chirp rate and remains constant over time. Therefore, the optimum delay to achieve the desired THz frequency f_{THz} is given by:

$$\Delta t = \frac{\pi f_{THz}}{\beta} \tag{3}$$

The central frequency of the THz frequency generated in a PPLN can be chosen by setting the poling period Λ [11] according to the phase matching condition:

$$f_{thz} = \frac{c}{\Lambda\,|n\,(f_{thz}) - n_g|} \tag{4}$$

where c is the speed of light, Λ is the poling period, $n\,(f_{thz})$ and n_g are the phase and the group refractive indices of both the THz waves and the pump. To maximize THz generation via chirped and delayed laser pulses experimentally, the delay Δt is adjusted so that the beat frequency matches the poling period of the PPLN. A poling period of 223 µm yields a central frequency of 480 GHz (Fig. 4a blue curve).

In a waveguide geometry with a cross-section comparable to the sub-THz wavelength (500 × 500 μm^2), the effective refractive index for the fundamental TE_{00} mode slightly deviates from the refractive index of the bulk crystal. This difference induces a small shift in the generated THz frequency compared to a bulk configuration. To evaluate this effect, we performed numerical simulations using COMSOL Multiphysics to extract the modal properties of the LN waveguide surrounded by air. Figure 4b shows the spatial distribution of the TE_{00} electric field at 480 GHz, using an extraordinary refractive index of 4.938 of the bulk crystal, obtained from the Lorentz-Drude model [29]. This polarization has been chosen to excite the d_{33} coefficient. The mode is well confined within the waveguide, with negligible leakage into the surrounding air. When substituting the bulk

refractive index in Eq. (2) with the effective refractive index of the TE_{00} mode, the predicted THz frequency shifts from 480 to 488 GHz. This shift confirms the impact of the waveguide geometry on the phase matching condition, which results from the small variation between the effective and bulk refractive indices.

Then, this study aims to achieve efficient THz wave generation under low pump power conditions by optimizing key parameters, namely the pulse duration, pump energy and pump beam geometry (collimated or focused pumping). To this end, we initiate our investigation by numerically solving the coupled propagation equations for both the optical and THz spectral components along the positive direction as described [14, 31]:

$$\begin{aligned}\frac{\mathrm{dA_{THz}}(\Omega,\mathrm{z})}{\mathrm{dz}} = & -\frac{\alpha(\Omega)}{2}\mathrm{A_{THz}}(\Omega,\mathrm{z}) \\ & -\frac{\mathrm{j}\Omega^2\chi^{(2)}_{eff}(\mathrm{z})}{2\mathrm{k}(\Omega)\mathrm{c}^2}\Psi(\mathrm{z}) \\ & \int \mathrm{A_{op}}(\omega+\Omega,\mathrm{z})\,\mathrm{A^*_{op}}(\omega,\mathrm{z})\,\mathrm{e}^{-\mathrm{j}[(\mathrm{k}(\omega+\Omega)-\mathrm{k}(\omega)-\mathrm{k}(\Omega)]\mathrm{z}}\mathrm{d}\omega\end{aligned} \tag{5}$$

$$\begin{aligned}\frac{\mathrm{dA_{op}}(\omega,\mathrm{z})}{\mathrm{dz}} = & -\frac{\mathrm{j}\omega^2\chi^{(2)}_{eff}(\mathrm{z})}{2k(\omega)c^2}\Psi(\mathrm{z}) \\ & \int \mathrm{A_{op}}(\omega+\Omega,\mathrm{z})\,\mathrm{A^*_{THz}}(\Omega,\mathrm{z}) \\ & \mathrm{e}^{-\mathrm{j}[(\mathrm{k}(\omega+\Omega)-\mathrm{k}(\omega)-\mathrm{k}(\Omega)]\mathrm{z}}\mathrm{d}\Omega \\ & -\frac{\mathrm{j}\omega^2\chi^{(2)}_{eff}(\mathrm{z})}{2\mathrm{k}(\omega)\mathrm{c}^2}\Psi \\ & \int \mathrm{A_{op}}(\omega-\Omega,\mathrm{z})\,\mathrm{A^*_{THz}}(\Omega,\mathrm{z}) \\ & \mathrm{e}^{-\mathrm{j}[(\mathrm{k}(\omega)-\mathrm{k}(\omega+\Omega)-\mathrm{k}(\Omega)]\mathrm{z}}\mathrm{d}\Omega \\ & +\mathrm{F}\left\{\frac{\mathrm{j}\varepsilon_0\omega_0\mathrm{n}(\omega_0)\mathrm{n}_2}{2}\,\mathrm{A_{op}}(\mathrm{t},\mathrm{z})\;|\mathrm{A_{op}}(\mathrm{t},\mathrm{z})|\right\} \\ & +\mathrm{F}\left\{\frac{\mathrm{j}\varepsilon_0\omega_0\mathrm{n}(\omega_0)\mathrm{n}_2}{2}\right. \\ & \left.\left[|\mathrm{A_{op}}(\mathrm{t}-\mathrm{t}',\mathrm{z})|^2\otimes\mathrm{h_r}(\mathrm{t}')\right]\;\mathrm{A_{op}}(\mathrm{t},\mathrm{z})\right\}\end{aligned} \tag{6}$$

$A_{THz}(\Omega,z)$ and $A_{op}(\omega,z)$ denote the electric field in the spectral domain of the THz and the optical waves, respectively. At the input of the crystal, $A_{THz}(\Omega,z=0)$ is null. The LN crystal is characterized by a frequency dependent absorption coefficient at room temperature $\alpha(\Omega)$, calculated from the from the Lorentz-Drude model [29], a second order nonlinear coefficient $\chi^{(2)}_{eff}$ = 336 pm/V and a second order nonlinear refractive index $n_2 = 1.25\times10^{-19}$ W/m^2 [14]. The parameter $\Psi(\mathrm{z}) = \frac{|\iint \mathrm{A_{op}}\mathrm{A_{THz}}dxdy|^2}{\iint|\mathrm{A_{op}}|^2dxdy\iint|\mathrm{A_{THz}}|^2dxdy}$ accounts for the integral overlap (IO) between the optical pump and THz fields. dx and dy denote integration over the transverse spatial coordinates of the beam cross-section (the plane perpendicular to the propagation direction z) [31]. This parameter remains constant for a collimated pump but varies along the z-axis when the pump field is focused. For a collimated beam, the IO is approximately unity. When the optical beam is focused, the minimum IO values are 0.99, 0.89, 0.78, and 0.63 for focal lengths of 750, 500, 400, and 300 mm, respectively. In the latter case, the optical beam size is updated at each propagation step based on a Gaussian beam evolution. $\Psi(z)$ and $A_{op}(\omega,z)$ are correspondly adjusted. The Raman contribution is described by $\mathrm{h_r}(t\prime)$ with $\mathrm{h_r}(t\prime) = F^{-1}\left\{\mathrm{h_r}\left(\omega'\right)\right\}$, where $\mathrm{h_r}\left(\omega'\right)$ is the stimulated Raman scattering transfer function [32]. Here F^{-1} represents the inverse Fourier transform. ε_0 and c represent the vacuum permittivity and the speed of light respectively. The carrier wave has a propagation constant k. Details on the physical processes described in Eqs. 5, 6 can be found in references [14, 30].

The coupled equations were numerically solved using a fourth-order Runge–Kutta method with spectral (Δω) and longitudinal (Δz) resolutions of 5 GHz and 11 µm respectively. To verify the accuracy of these results, addition simulations with finer resolution (Δω = 1 GHz and Δz = 5 µm) were performed, confirming consistent results. The 5 GHz and 11 µm setting was used chosen to optimize computational efficiency.

3 Results

3.1 Simulation results

By solving Eqs. (3) and (4), we first analyzed the THz generation efficiency for various pulse durations, ranging from 5 to 30 ps as the function of the waveguide length. According to Eq. 3, varying the pulse duration within this range correspondingly adjusts the relative time delay, ranging from 2 to 12.5 ps. As shown in Fig. 5a, for a pump energy of 0.1 µJ and a pump spectral bandwidth of 6 nm centered at 1025 nm, the optimal THz generation is achieved with a pulse duration of 5 ps using a Gaussian beam with a diameter of 565 µm fully illuminating the crystal's cross-section. This optimal efficiency arises from a balance between pulse duration, intensity, and the temporal overlap of the delayed chirped pulses. Shorter pulses provide higher peak intensity and a shorter delay between pulses, ensuring better temporal overlap of the delayed pulses and enhanced nonlinear interaction, both critical for efficient THz generation. Conversely, longer pulses reduce the intensity and increase the relative delay, leading to insufficient overlap and reducing efficiency. However, longer pulses offer the advantages of producing narrower-band THz spectra as shown in Fig. 5b, c. For example, at z = 550 µm, the THz spectrum is notably narrower for τ = 30 ps (inset, Fig. 5c) compared to τ = 5 ps (inset, Fig. 4b). Another advantage of using longer pulses

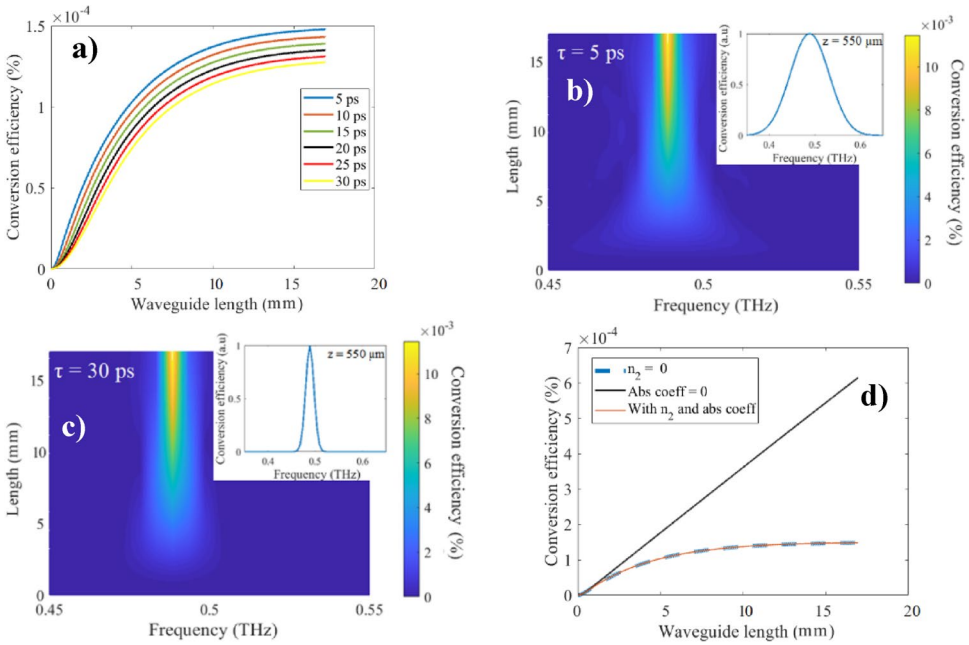

Fig. 5 **a** Efficiency as a function of the waveguide's length for different pulse durations and a collimated beam; Energy = 0.1 μJ and Gaussian beam diameter of 565 μm. **b** Efficiency as a function of the frequency and crystal length for τ = 5 ps. The inset represents the efficiency as a function of the frequency for z = 550 μm. **c** Efficiency as a function of the frequency and crystal length for τ = 30 ps. The inset represents the efficiency as a function of the frequency for z = 550 μm. **d** Efficiency as a function of the PPLN length for a pulse duration of 5 ps when different parameters are switched on and off

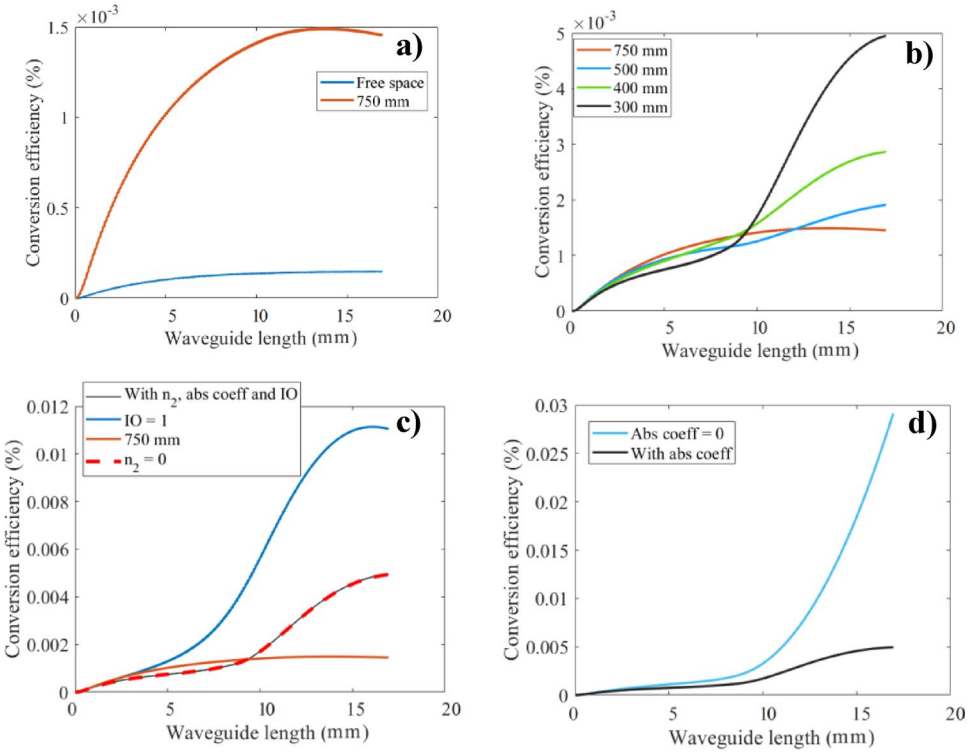

Fig. 6 Efficiency as a function of the waveguide's length for an energy of 0.1 μJ and for **a** focused beam using 750 mm lens and collimated beam. **b** Different lenses. **c** 750 mm and 300 mm lenses when different parameters are switched on and off. **d** 300 mm lens with and without absorption coefficient

is the ability to maximize the optical pulse energy without exceeding the intensity damage threshold of the crystal.

In Fig. 5d, we examine the efficiency saturation observed with 5 ps pulses, which begins at a waveguide length of 1.5 cm (Fig. 5a). To identify the saturation mechanism, we ran simulations disabling nonlinear effects such as SPM and Raman scattering by removing n_2 (dashed blue curve). The resulting efficiency closely matches the original curve (orange), indicating that these nonlinearities are not responsible for the saturation. However, when setting the absorption coefficient $\alpha = 0$ (black curve), the efficiency scales linearly with the waveguide length, revealing that absorption is the dominant factor limiting efficiency in this regime.

In Fig. 6a, we compare the THz generation efficiency for two pump configurations: a collimated beam with a 565 μm diameter and a focused beam using a 750 mm focal length lens, where the focus is positioned at the center

of the waveguide. The pump energy is also set at 0.1 µJ. For the focused configuration, the variation of the optical spectral envelope along the propagation axis z is explicitly accounted for in Eqs. (5) and (6) by modeling the evolution of the beam size and intensity due to focusing. The input beam radius before the lens is 2 mm, matching the actual laser beam diameter used in the experimental setup. As a result, the highest intensity occurs at the focus (in the Rayleigh range), with progressively lower intensities at the waveguide entrance and exit. This spatial intensity profile directly influences the nonlinear interaction and the resulting THz generation efficiency. At a waveguide length of 16 mm, the collimated pump configuration yields a THz generation efficiency of approximately 1.5×10^{-4}%, whereas the focused beam configuration achieves a significantly higher efficiency of about 1.5×10^{-3}%, representing a tenfold improvement. This enhancement results from the favorable trade-off between higher pump intensity and the reduced spatial overlap between the pump and THz waves within the waveguide when using a focused beam. However, for lengths exceeding 15 mm, the efficiency starts to decline due to THz absorption in the LN crystal. In Fig. 6b, we further explore the efficiency dependence on the focusing geometry by employing lenses with focal lengths of 750, 500, 400 and 300 mm, corresponding to beam waists of 122.3, 81.5, 65.2 and 48.9 µm respectively, at the focus point. Lenses with longer focal lengths provide better spatial overlap but deliver lower pump intensity. For longer waveguides, shorter focal lengths (i.e., tighter focusing) yield higher efficiency due to the increased intensity. For example, using a 300 mm lens results in an efficiency of about 5×10^{-3}%, roughly four times higher than that achieved with a 750 mm lens. However, for shorter waveguides (less than 8 mm), lenses with longer focal lengths offer better efficiency than shorter focal length lenses.

To investigate the origin of this behavior, we analyze Fig. 6c, where efficiency is plotted against waveguide length for different cases: A 300 mm lens with all effects included (black curve); the same 300 mm lens with SPM and Raman processes disabled ($n_2 = 0$, dashed red curve); the 300 mm lens with the IO artificially set to 1 (blue curve); the 750 mm lens with all parameters included (orange curve).The close match between the $n_2 = 0$ case and the original curve confirms that SPM and Raman processes do not significantly influence the efficiency drop. However, when the integral overlap is set to 1, the efficiency notably increases compared to both the original 300 mm lens curve and the 750 mm lens case. This observation indicates that for waveguide lengths shorter than 8 mm, the efficiency drop primarily stems from a reduction in spatial overlap (integral overlap) between the pump and THz fields when using shorter focal length lenses. Finally, in Fig. 6d, we compare results for the 300 mm lens configuration with and without including THz absorption. The pronounced decrease in efficiency and saturation onset beyond 15 mm is confirmed to be mainly caused by THz absorption in LN.

In Fig. 7a, we evaluate the THz generation efficiency as a function of pump energy for lenses with focal lengths

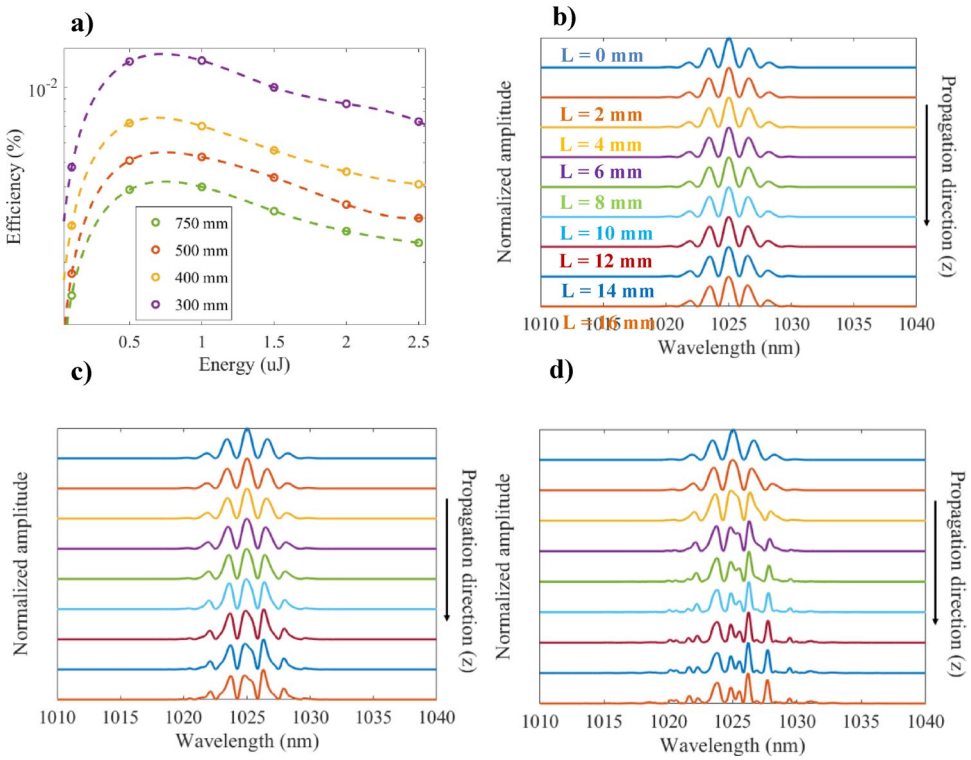

Fig. 7 **a** Efficiency as a function of the energy for different lenses. **b** optical spectrum along the waveguide, sampled every 2.2 mm for energy value of 0.1 µJ. **c** 0.5 µJ. **d** 2.5 µJ. The curves are vertically shifted for clarity

ranging from 750 to 300 mm, measured at z = 16 mm. We remind that the beam size evolves with the propagation and therefore the intensity is modified for each longitudinal step. The results show that efficiency improves as the focal length decreases, due to a better balance between increased pump intensity at the focus position and reduced integral overlap between the pump and THz waves. Additionally, efficiency increases with pump energy up to 0.5 µJ, reaches a plateau between 0.5 and 1 µJ, and then declines at energies above 1 µJ. The highest efficiency, approximately 1.2×10^{-2}%, is achieved with the 300 mm lens in the 0.5–1 µJ energy range. To investigate the observed efficiency decrease at higher pump energies, we analyzed the normalized optical spectra along the waveguide, sampling every 2 mm (with L = 0 mm at the top and L = 16 mm at the bottom), for pump energies of 0.1 µJ (Fig. 7b), 0.5 µJ (Fig. 7c), and 2.5 µJ (Fig. 7d), using the 300 mm lens. At 0.1 µJ (Fig. 7b), the optical spectrum remains unchanged along the waveguide, indicating negligible nonlinear effects such as SPM, stimulated Raman scattering, or cascading via difference- and sum-frequency generation between the optical and THz fields. At 2.5 µJ (Fig. 7d), however, significant spectral broadening is observed, starting around 6 mm, resulting from both cascading processes and SPM. In comparison, at 0.5 µJ (Fig. 7c), spectral modifications appear later—around 14 mm. The early onset of spectral changes at high energies, particularly in the 2.5 µJ case, leads to reduced efficiency when the pump reaches 16 mm. These spectral modifications alter the phase-matching conditions, ultimately lowering the efficiency of THz generation.

3.2 Experimental results and discussion

Based on numerical simulations, the optimal parameters for efficient THz generation in a PPLN crystal with a 223 µm poling period and a 1.6 cm length were identified as a 5 ps pulse duration and a 1 µJ pump energy, focused using a 300 mm focal length lens. Figure 8 presents the schematic of the corresponding experimental setup.

Ultrashort femtosecond pulses were generated by an Ytterbium laser, operating at a central wavelength of 1025 nm with an 85 kHz repetition rate. A beam splitter divided the pulse into pump and probe beams. The pump beam was directed to a parallel grating pair chirped pulse stretcher, where the grating angle and spacing were optimized to produce a pulse duration of 5 ps with minimal losses. The pulse duration was measured before and after stretching using a non colinear autocorrelator, as shown in Fig. 9a, where the green curve represents the pulse before stretching (τ ~ 210 fs). Blue curve shows the pulse after stretching. The stretched pulse was fitted with a Gaussian profile (dashed orange curve), confirming a pulse duration of approximately 5 ps. Following the stretcher, a Michelson interferometer split the pulse into two identical copies with adjustable relative delay. The delay between the pulses was finely controlled using a delay stage in one arm of the interferometer. Using Eq. 3, we calculated a delay of 2.2 ps, between the two pulses to obtained a frequency difference of 488 GHz optimized for the PPLN. The interference of these two pulses creates a spectral beating in the frequency domain, independently of β, with a spacing of 1.5 nm. For comparison, a spectrum was numerically calculated under the same parameters and is shown as the dashed orange curve in Fig. 9b. It confirms the expected modulation with the correct spectral beating.

The two linearly chirped and delayed pulses were first directed to a spectrometer, with the delay stage in the Michelson interferometer adjusted to achieve a beating frequency of approximately 1.5 nm, as shown in Fig. 9b (blue curve). The beam was then focused at the center of the

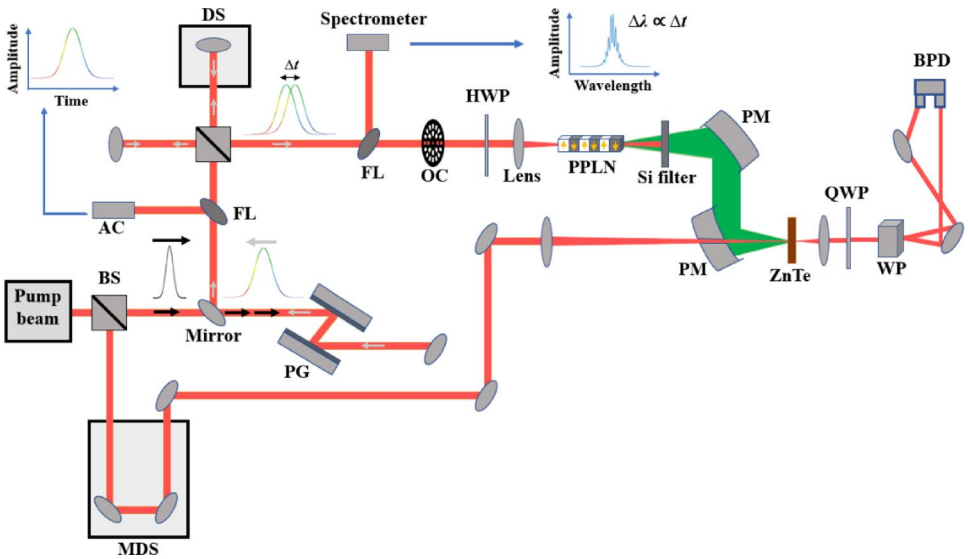

Fig. 8 Schematics of the experimental setup. BS: Beam splitter; PG: Parallel grating; MDS: Motorized delay stage; FL: Folding mirror; DS: Delay stage; AC: autocorrelator; OC: Optical chopper; HWP: Half wave plate; PM: Parabolic mirror; QWP: Quarter wave plate; WP: Wollaston prism; BPD: Balanced photodetector

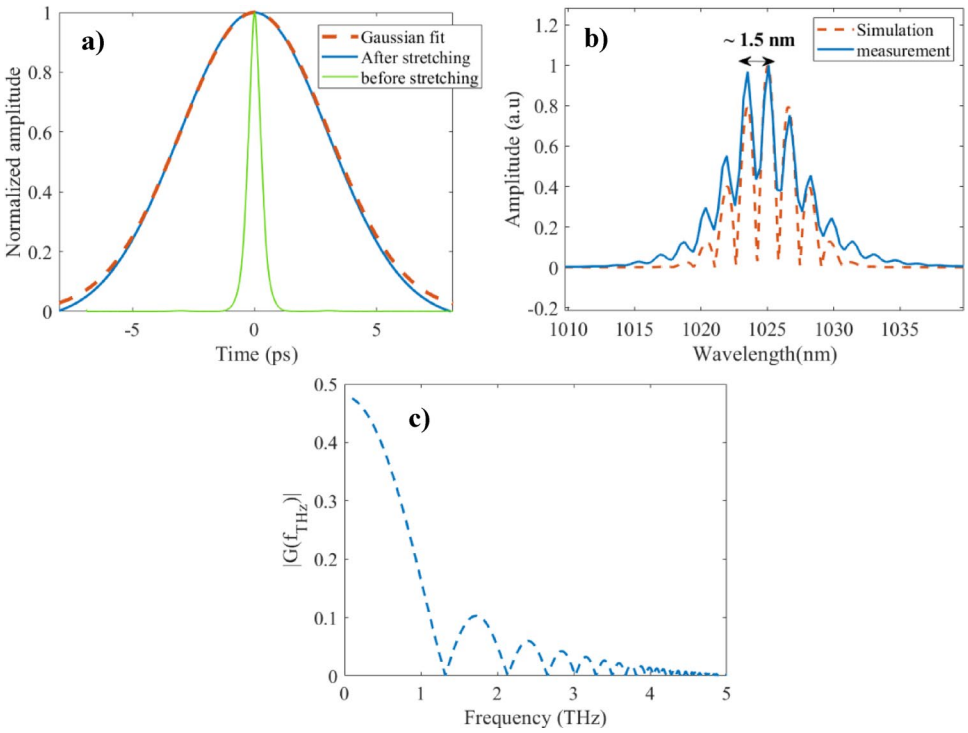

Fig. 9 **a** Temporal profile of the optical pulse, both before and after the stretching process. (Dashed orange curve shows the Gaussian fit for the stretched pulse). **b** The optical spectrum of the two linearly stretched pulses separated by 2.2 ps. **c** Electro-optic response of 1 mm thick ZnTe crystal at 1025 nm

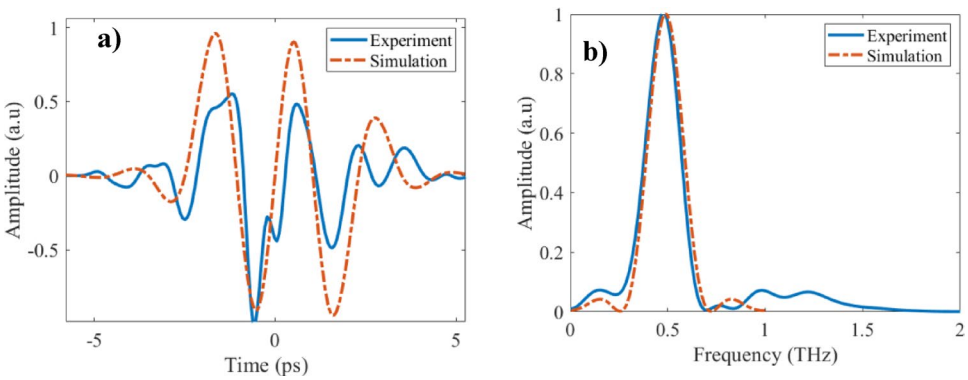

Fig. 10 **a** Temporal waveform of the THz field. **b** Corresponding normalized spectral profile

PPLN waveguide using a 300 mm focal length lens. Inside the PPLN, THz waves were generated and guided by total internal reflection along the waveguide until reaching the output facet. At the output, the THz waves were collimated and directed by a pair of 2-inch off-axis parabolic mirrors coated with protected aluminum. To eliminate any residual pump light, a thin high-resistivity silicon substrate served as a low-pass filter. Finally, the temporal electric field of the THz waves was measured using electro-optic (EO) sampling, where the probe beam was overlapped both temporally and spatially with the THz field inside a 1 mm-thick zinc telluride (ZnTe) crystal, whose electro-optic response is shown in Fig. 9c [33], spanning up to 1.3 THz and ensuring that the setup can effectively capture and fully characterize the temporal and spectral features of the generated THz field centered at 488 GHz.

The blue curve in Fig. 10a shows the THz waveform measured by EO sampling at a pump energy of 1 µJ. The waveform exhibits several cycles with an approximate period of 2 ps, consistent with a sub-THz frequency. The blue curve in Fig. 10b represents the corresponding Fourier transform of the temporal electric field. It reveals a spectrum centered at 488 GHz with a bandwidth of ~ 180 GHz. This experimental result agrees well with the prediction from Eq. (4), which estimated a central frequency of 488 GHz based on the effective refractive indices of the PPLN waveguide.

The simulated temporal and spectral profiles are presented in Fig. 11. The simulated temporal waveform (Fig. 11a) shows a multicycle oscillation, leading to a narrow spectral bandwidth of a few GHz (Fig. 11b). In contrast, the experimental measurements exhibit fewer visible cycles in the temporal profile (Fig. 10a), resulting in a broader spectral bandwidth (Fig. 10b). This discrepancy in bandwidth

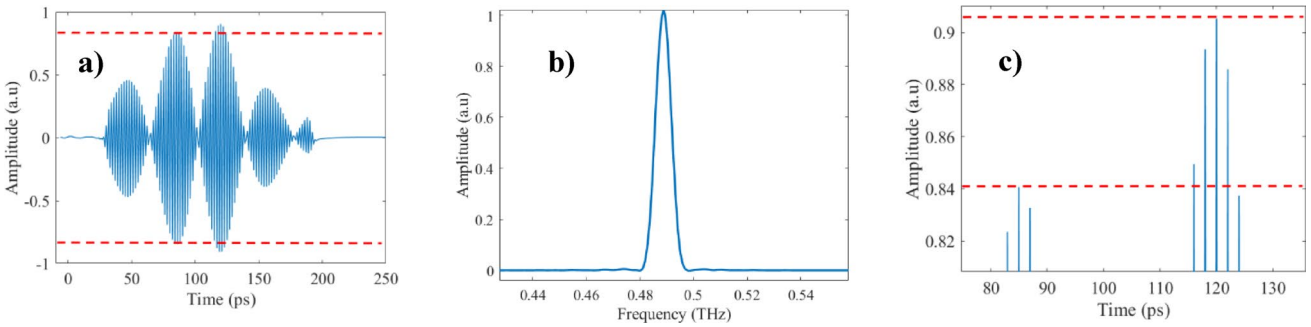

Fig. 11 **a** Numerical temporal electric field of the THz waves with dashed red lines showing the noise background. **b** Corresponding THz spectrum. **c** Zoomed-in view for amplitudes above the noise background

Fig. 12 **a** Temporal electric field of the THz waves pumped using a 750 mm lens. **b** Corresponding normalized spectral profile

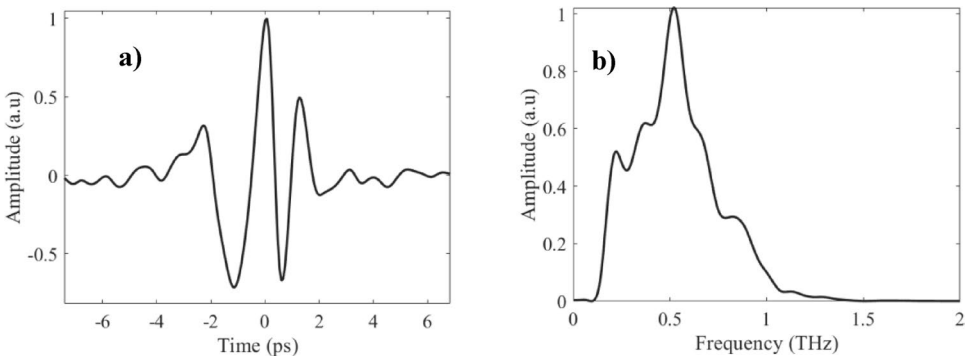

likely arises from the limited dynamic range of the experimental detection system. In the measured waveform, only the cycles with the highest amplitudes—corresponding to the strongest part of the simulated field—are effectively detected. Oscillations with lower amplitudes fall below the system's noise floor during electro-optic sampling, making them indistinguishable from noise.

To illustrate this effect, a time-domain gating operation was applied to the simulated waveform, in which the field amplitude was set to zero outside the 116.9–122.9 ps interval and retained within this window (Fig. 11a). The red dashed lines in Fig. 11a indicate the amplitude threshold corresponding to the experimental detection limit. Only oscillation cycles exceeding this threshold were retained. The threshold was defined such that the temporally resolved portion of the simulated electric field reproduces the experimentally measured waveform. A magnified view of the cycles above this detection threshold is shown in Fig. 11c. The resulting gated numerical waveform (orange curve in Fig. 10a) reproduces the main temporal feature observed experimentally (blue curve).

Furthermore, the Fourier transform of this filtered numerical waveform, shown as the dashed orange curve in Fig. 10b, reveals a normalized spectrum centered at 488 GHz with a bandwidth of approximately 180 GHz. This matches well with the experimental spectrum (blue curve), confirming that the observed spectral broadening stems primarily from the limited detection sensitivity, which allows only the higher amplitude cycles of the generated THz waveform to be recorded.

To further examine this assumption, the pump intensity was reduced by employing a 750 mm focal length lens. This configuration results in a lower intensity compared to the 300 mm lens, which is expected to yield a broader detected spectrum due to the weaker nonlinear interaction. The corresponding THz temporal waveform is shown in Fig. 12a and reveals fewer oscillation cycles than those obtained with the 300 mm lens. The Fourier transform of this waveform, presented in Fig. 12b, shows a spectrum centered around 500 GHz, consistent with the value dictated by the poling period of the PPLN waveguide. However, the detected spectral bandwidth is significantly and artificially broader than that observed with the 300 mm lens. Specifically, while the 300 mm lens configuration yields a spectrum spanning 0.3–0.6 THz, the 750 mm lens produces a much broader spectrum extending approximately from 0.1 to 1.3 THz. The fact that the central frequency remains near 488 GHz confirms that the generation mechanism is governed by the poling period of the PPLN waveguide. In contrast, the observed spectral broadening highlights the limitations of the detection system's sensitivity, which fail to resolve lower amplitude oscillations, especially at reduced pump intensities. These findings underscore that the detection setup constrains the accurate characterization of the generated THz spectrum, particularly under low-intensity conditions,

where significant portions of the waveform may remain undetected due to the system's noise floor.

The experimental efficiency was not measured because the THz power was below the detection limit of our pyroelectric detector (10 μW). Since the detected power is < 10 μW, the corresponding efficiency is therefore lower than 10^{-4}.

4 Conclusion

In summary, we have numerically optimized and experimentally demonstrated THz generation using chirped and delayed laser pulses in a compact system operating under low-power pumping with a PPLN waveguide. Numerical simulations identified the optimal parameters for a 16 mm-long PPLN with a 223 μm poling period as a pump energy of 1 μJ, a pulse duration of 5 ps, and a 300 mm focusing lens. Experimental results revealed a narrow-band THz spectrum with a bandwidth of 180 GHz centered at 488 GHz, in good agreement with both the PPLN poling period and numerical predictions. Although the detected spectral bandwidth is currently limited by the sensitivity of the detection setup, we anticipate that cooling the PPLN to cryogenic temperatures could further enhance efficiency [12]. Additionally, exploring PPLN waveguides with reduced cross-sectional geometries may provide opportunities to improve efficiency by balancing the THz mode confinement with the number of supported modes. These findings establish a pathway toward efficient, low-power THz generation using waveguided based integrated nonlinear optical platforms.

Author contributions Conceptualization, IB, MD, SD,CFD,VR,MC and DB; methodology, IB, MD, SD,GT,FF,MEO,CFD,VR,MC and DB; software, IB, MD, CFD, DB and MC.; validation, all authors.; formal analysis, IB, MD,SD.; investigation, all authors; resources, SD, FF,MC, HM, PM and DB.; data curation, HM,VR,MC, PM and DB.; writing—original draft preparation, I.B, S.D; writing—review and editing, all authors; supervision, HM,VR, MC, PM and DB.; project administration, H.M, MC,SD and DB funding acquisition, SD, HM, MC, PM and DB, All authors have read and agreed to the published version of the manuscript.

Funding This research was funded by IdEx University of Bordeaux/ Grand Research Program LIGHT (ANR-10-IDEX-0003); ISITE BFC (ANR-15-IDEX-03); EIPHI Graduate School (ANR-17-EURE-0002); EQUIPEX+SMARTLIGHT platform (ANR-21-ESRE-0040), Conseil Régional de Bourgogne-Franche-Comté; French RENATECH Network and its Mimento Technological Facility; Nano-FiLN project (ANR-23-PEEL-0004).

Data availability Data underlying the results presented in this paper are not publicly available at this time but may be obtained from the authors upon reasonable request.

Declarations

Conflict of interest The authors declare no competing interests.

References

1. V. Kumar, P. Mukherjee, L. Valzania, A. Badon, P. Mounaix, S. Gigan, Fourier synthetic-aperture-based time-resolved terahertz imaging. Photon. Res. **13**(2), 407–416 (2025)
2. Q. Cassar, S. Caravera, G. MacGrogan, T. Bücher, P. Hillger, U. Pfeiffer, T. Zimmer, J.P. Guillet, P. Mounaix, Terahertz refractive index-based morphological dilation for breast carcinoma delineation. Sci. Rep. **11**(1), 6457 (2021)
3. D. Bigourd, G. Mouret, A. Cuisset, F. Hindle, E. Fertein, R. Bocquet, Rotational spectroscopy and dynamics of carbonyl sulphide studied by terahertz free induction decays signals. Opt. Commun. **281**, 3111–3119 (2008)
4. N. Inomata, T. Takahashi, Y. Sakai, T. Okatani, Y. Kanamori, Fabrication and application of 3D Terahertz metamaterials with vertical multi nanogaps for spectroscopic sensing. Sci. Rep. **15**, 13636 (2025)
5. D. Zhang, M. Fakhari, H. Cankaya, A.L. Calendron, N.H. Matlis, F.X. Kärtner, Cascaded multicycle terahertz-driven ultrafast electron acceleration and manipulation. Phys. Rev. X **10**, 011067 (2020)
6. S. Koenig, D. Lopez-Diaz, J. Antes, F. Boes, R. Henneberger, A. Leuther, A. Tessmann, R. Schmogrow, D. Hillerkuss, R. Palmer, T. Zwick, C. Koos, W. Freude, O. Ambacher, J. Leuthold, I. Kallfass, Wireless sub-THz communication system with high data rate. Nat. Photon. **7**, 977 (2013)
7. M.E. Ojo, F. Fauquet, P. Mounaix, D. Bigourd, THz pulse generation and detection in a single crystal-layout. Photonics **10**, 316 (2023)
8. G. Taton, F. Fauquet, I. Betka, J.P. Guillet, F. Darracq, P. Mounaix, D. Bigourd, Broadband THz emission of long pulses from photomixing process with optical chirped pulses. Opt. Lett. **50**(2), 650 (2025)
9. I. Betka, M. Deroh, M.E. Ojo, F. Fauquet, C. Fourcade-dutin, H. Maillotte, M. Chauvet, P. Mounaix, D. Bigourd, Generation of broadband THz radiation by polariton parametric scattering in a LiNbO3 waveguide. Opt. Continuum **4**, 687 (2025)
10. Z. Chen, X. Zhou, A. Werley, K.A. Nelson, Generation of high power tunable multicycle teraherz pulses. Appl. Phys. Lett. **99**(7), 071102 (2011)
11. F. Ahr, S.W. Jolly, N.H. Matlis, S. Carbajo, T. Kroh, K. Ravi, D.N. Schimpf, J. Schulte, H. Ishizuki, T. Taira, A.R. Maier, F.X. Kärtner, Narrowband terahertz generation with chirped-and-delayed laser pulses in periodically poled lithium niobate. Opt. Lett. **42**, 2118 (2017)
12. S.W. Jolly, N.H. Matlis, F. Ahr, V. Leroux, T. Eichner, A.L. Calendron, H. Ishizuki, T. Taira, F.X. Kärtner, A.R. Maier, Spectral phase control of interfering chirped pulses for high-energy narrowband terahertz generation. Nat. Commun. **10**, 2591 (2019)
13. B.N. Carnio, A.Y. Elezzabi, Enhanced broadband terahertz radiation generation near the reststrahlen band in sub-wavelength leaky-mode LiNbO3 waveguides. Opt. Lett. **43**, 1694 (2018)
14. K. Ravi, D.N. Schimpf, F.X. Kärtner, Pulse sequences for efficient multi-cycle terahertz generation in periodically poled lithium niobate. Opt. Express **24**, 25582 (2016)
15. D. Jang, K.Y. Kim, Multicycle terahertz pulse generation by optical rectification in $LiNbO_3$, $LiTaO_3$, and BBO crystals. Opt. Express **28**, 21220 (2020)
16. E. Singh, M.N. Ekta, S. Reitzig, M. Lange, M. Rüsing, L.M. Eng, S. Sanna, Vibrational properties of $LiNbO_3$ and $LiTaO_3$ under uniaxial stress. Phys. Rev. Mater. **7**, 024420 (2023)
17. L.E. Myers, R.C. Eckardt, M.M. Fejer, R.L. Byer, W.R. Bosenberg, J.W. Pierce, Quasi-phase-matched optical parametric oscillators in bulk periodically poled $LiNbO_3$. J. Opt. Soc. Am. B Opt. Phys. **12**, 2102 (1995)

18. Y.-S. Lee, T. Meade, V. Perlin, H. Winful, T.B. Norris, A. Galvanauskas, Generation of narrow-band terahertz radiation via optical rectification of femtosecond pulses in periodically poled lithium niobite. Appl. Phys. Lett. **76**, 2505 (2000)
19. B.N. Carnio, O. Moutanabbir, E.Z. Elezzabi, Nonlinear photonic waveguides: a versatile platform for terahertz radiation generation (a review). Laser Photon. Rev. **17**, 2200138 (2023)
20. I.F. Akyildiz, J.M. Jornet, C. Han, Terahertz band: next frontier for wireless communications. Phys. Commun. **12**, 16 (2014)
21. X. Wu, H. Lu, K. Sengupta, Programmable terahertz chip-scale sensing interface with direct digital reconfiguration at sub-wavelength scales. Nat. Commun. **10**, 2722 (2019)
22. B.S. Dastrup, E.R. Sung, F. Wulf, C. Saraceno, K. Nelson, Enhancement of THz generation in $LiNbO_3$ waveguides via multi-bounce velocity matching. Light Sci. Appl. **11**, 335 (2022)
23. M. Chauvet, F. Henrot, F. Bassignot, F. Devaux, L. Gauthier-Manuel, V. Pêcheur, H. Maillotte, B. Dahmani, High efficiency frequency doubling in fully diced LiNbO3 ridge waveguides on silicon. J. Opt. **18**, 085503 (2016)
24. V. Pecheur, H. Porte, J. Hauden, F. Bassignot, M. Deroh, M. Chauvet, Watt-level SHG in undoped high step-index PPLN ridge waveguides. OSA Continuum **4**, 1404 (2021)
25. C. Courdurié, S. Dubuis, T. Buffeteau, J.-P. Salvetat, F. Adamietz, E. Genin, V. Rodriguez, L. Vellutini, Highlighting structure-dependent orientational interactions between azobenzenes within second harmonic generation-active self-assembled monolayers. J. Phys. Chem. C (2025). https://doi.org/10.1021/acs.jpcc.5c03795
26. V.G. Dmitriev, G.G. Gurzadyan, D.N. Nikogosyan, *Handbook of Nonlinear Optical Crystals*, 2nd edn. (Springer, Berlin, 1997)
27. A. Cartella, T.F. Nova, A. Oriana, G. Cerullo, M. Först, C. Manzoni, A. Cavalleri, Narrowband carrier-envelope phase stable mid-infrared pulses at wavelengths beyond 10 μm by chirped-pulse difference frequency generation. Opt. Lett. **42**, 663 (2017)
28. A.S. Weling, B.B. Hu, N.M. Froberg, D.H. Auston, Generation of tunable narrow-band THz radiation from large aperture photoconducting antennas. Appl. Phys. Lett. **64**, 137 (1994)
29. A.J. Lee, D.J. Spence, H.M. Pask, Terahertz sources based on stimulated polariton scattering. Prog. Quantum Electron. **71**, 100254 (2020)
30. K. Ravi, W.R. Huang, S. Carbajo, X. Wu, F. Kärtner, Limitations to THz generation by optical rectification using tilted pulse fronts. Opt. Express **22**, 20239 (2014)
31. G. Agrawal, Nonlinear Fiber Optics, 5 ed (Academic 2013).
32. C.R. Phillips, C. Langrock, J.S. Pelc, M.M. Fejer, I. Hartl, M.E. Fermann, Supercontinuum generation in quasi-phase matched waveguides. Opt. Express **19**, 18754 (2011)
33. Q. Wu, X.-C. Zhang, 7 terahertz broadband GaP electro-optic sensor. Appl. Phys. Lett. **70**, 1784 (1997)